

# Structure and Morphology Development in Syndiotactic Polypropylene during Isothermal Crystallization and Subsequent Melting

ZHI-GANG WANG,<sup>1</sup> XUE-HUI WANG,<sup>1</sup> BENJAMIN S. HSIAO,<sup>1</sup> ROGER A. PHILLIPS,<sup>2</sup>  
FRANCISCO J. MEDELLIN-RODRIGUEZ,<sup>1</sup> SRIVATSAN SRINIVAS,<sup>3</sup> HOWARD WANG,<sup>4</sup> CHARLES C. HAN<sup>4</sup>

<sup>1</sup>Department of Chemistry, State University of New York at Stony Brook, Stony Brook, New York 11794-3400

<sup>2</sup>R&D Center, Basell USA Incorporated, 912 Appleton Road, Elkton, Maryland 21921

<sup>3</sup>Baytown Polymers Center, ExxonMobil Chemical Company, Baytown, Texas 77522-5200

<sup>4</sup>Polymers Division and Center for Neutron Research, National Institute of Standards and Technology, Gaithersburg, Maryland 20899

*Received 30 January 2001; revised 29 August 2001; accepted 14 September 2001*

**ABSTRACT:** Structure and morphology development during the isothermal crystallization and subsequent melting of syndiotactic polypropylene (sPP) was studied with differential scanning calorimetry (DSC), time-resolved simultaneous small-angle X-ray scattering (SAXS), and wide-angle X-ray diffraction (WAXD) methods with synchrotron radiation. The morphology of sPP isothermally crystallized at 100 °C for 3 h was also characterized with transmission electron microscopy (TEM). Time- and temperature-dependent parameters such as the long period ( $L$ ), crystal lamellar thickness ( $l_c$ ), amorphous layer thickness ( $l_a$ ), scattering invariant ( $Q$ ), crystallinity ( $X_c$ ), lateral crystal sizes ( $L_{200}$  and  $L_{010}$ ), and unit cell dimensions ( $a$  and  $b$ ) were extracted from the SAXS and WAXD data. Results indicate that the decreases in  $L$  and  $l_c$  with time are probably due to the formation of thinner crystal lamellae, and the decreases in  $a$  and  $b$  are due to crystal perfection. The changes in the morphological parameters ( $Q$ ,  $X_c$ ,  $L$ , and  $l_c$ ) during subsequent melting exhibited a two-stage process that was consistent with the multiple melting peaks observed in DSC. The two high-temperature peaks can be attributed to the melting of primary lamellae (at lower temperatures) and recrystallized lamellae (at higher temperatures). An additional minor peak, located at the lowest temperature, was also visible and was related to the melting of thin and defective secondary lamellae. TEM results are consistent with the SAXS data, which supports the assignment of the larger value ( $l_1$ ) from the correlation function analysis as  $l_c$ . WAXD showed that the thermal expansion was greater along the  $b$  axis than the  $a$  axis during melting. © 2001 John Wiley & Sons, Inc. *J Polym Sci Part B: Polym Phys* 39: 2982–2995, 2001

**Keywords:** syndiotactic polypropylene; crystal structures; morphology; isothermal crystallization; multiple melting; SAXS; wide-angle X-ray diffraction (WAXD)

## INTRODUCTION

Polypropylene has become one of the most useful commodity polymers today. It has many attrac-

tive properties, including a relatively low price. In semicrystalline polymers, the structure and morphology can directly affect the final properties. Thus, there has been a continuing interest in understanding the structure–property relationships of stereoregular polypropylenes.<sup>1–7</sup> Extensive studies have been carried out for isotactic polypropylene (iPP; e.g., ref. 2). In contrast, there

Correspondence to: B. S. Hsiao (E-mail: bhsiao@notes.cc.sunysb.edu)

*Journal of Polymer Science: Part B: Polymer Physics*, Vol. 39, 2982–2995 (2001)  
© 2001 John Wiley & Sons, Inc.

are fewer studies for syndiotactic polypropylene (sPP) because of the later development of highly syndioregular polypropylene.

Highly stereoregular sPP samples have been made available mainly because of the new metallocene-catalyst technology.<sup>8,9</sup> Several studies dealing with the morphology, crystalline structure, and thermal properties have been reported.<sup>10–17</sup> For the real-time development of structure and morphology, only a few studies exist. For example, Ohira et al.<sup>17</sup> investigated the crystal transformation and structural changes of the planar zigzag form (III) in sPP during the heating process by differential scanning calorimetry (DSC), wide-angle X-ray diffraction (WAXD), and high-resolution, solid-state <sup>13</sup>C NMR spectroscopy. Cheng et al.<sup>12</sup> studied the crystallization, melting, and morphology of sPP fractions by polarized light microscopy, electron diffraction, and WAXD. They reported that the dominant crystalline structure of sPP was spherulitic, even though the spherulite superstructure was restricted and the average dimension was small. They also investigated the *in situ* crystal growth and subsequent melting of sPP single crystals (grown from melt crystallization) with transmission electron microscopy (TEM) and atomic force microscopy.<sup>16</sup>

In this article, the time evolution of the structure and morphology during isothermal crystallization and subsequent melting in sPP is investigated by simultaneous small-angle X-ray scattering (SAXS) and WAXD techniques. SAXS was used to investigate the lamellar morphology, and WAXD was used to study the crystal unit cell information. DSC was also employed to monitor the heat flow during isothermal crystallization and melting; the results were compared with the changes in the structural and morphological parameters extracted from the X-ray data. TEM was further used to provide direct information on crystal lamellae in real space. The objective of this study is to provide a better understanding of the structural and morphological development during crystallization and melting in sPP.

## EXPERIMENTAL

The experimental sPP sample was prepared by a metallocene-catalyst process. The gel permeation chromatography data showed that the sPP sample had a number-average molecular weight ( $M_n$ ) of 86,100, a weight-average molecular weight ( $M_w$ ) of 173,900, a *z*-average molecular weight

( $M_z$ ) of 286,200, and an  $M_w/M_n$  value of 2.02.<sup>18</sup> The sPP sample exhibited a triad distribution of 4.00% (mass fraction) isotactic, 10.76% heterotactic, and 85.24% syndiotactic, as determined by NMR. The pentad [rrrrr] content in mass fraction was 69.39%. The NMR pentad distribution can be interpreted as containing 24 single unit stereoerrors per 1000 monomer units and 20 stereoinversions per 1000 monomer units. The analysis showed evidence for stereoerrors, probably due to both catalytic-site control and chain-end control. This analysis indicated that the chosen sPP sample was not highly stereospecific but instead was stereoblocky, with predominantly syndiotactic sequences and a small fraction of atactic sequences.

The samples were compression-molded into 1 mm thick and 7 mm diameter disks with a Carver press<sup>19</sup> at 160 °C for 5 min (under a pressure of 13.8 MPa) and were cooled to room temperature ( $\approx 25$  °C). Pinhole-collimated simultaneous SAXS and WAXD measurements were conducted at the Advanced Polymers Beamline X27C ( $\lambda = 1.307$  Å) at the National Synchrotron Light Source (Brookhaven National Laboratory). Two linear position-sensitive detectors (European Molecular Biology Laboratory) were configured for simultaneous data acquisition. Isothermal crystallization measurements were carried out with a dual-chamber temperature jump apparatus, which has been described elsewhere.<sup>20</sup> The sample was held at a temperature of 170 °C for 10 min to reach an equilibrium melt (the nominal melting temperature of sPP was 160 °C) and was jumped to temperatures of 73, 83, 93, 101, and 113 °C for crystallization measurements. The temperature fluctuation was  $\pm 0.5$  °C. The data collection times for 73, 83, 93, 101, and 113 °C were 20, 69, 95, 138, and 165 min, respectively. These measurement times were determined by the crystallization rate at each temperature. The measurement was terminated when the collected SAXS and WAXD signals were visually unchanged. Both X-ray profiles (SAXS and WAXD) were collected in 30 s increments. The data were normalized for incident beam fluctuations. The sample-to-detector distance for SAXS was 1460 mm. The SAXS angle was calibrated with a silver behenate standard. The WAXD pixel resolution and the intensity were calibrated by a comparison of the synchrotron data with the Siemens Hi-Star X-ray diffractometer data (Cu  $K\alpha$ ) collected in the  $\theta$ - $\theta$  reflection mode and corrected for detector nonlinearity and empty-beam scattering. The angular scale of the synchrotron WAXD data ( $\lambda = 1.307$  Å) was

converted to a scale corresponding to  $\lambda = 1.542 \text{ \AA}$  for presentation and discussion.

A PerkinElmer DSC7 instrument was used to collect the DSC scans. This instrument was calibrated with an indium standard (at  $20 \text{ }^\circ\text{C/min}$ ). The samples used for DSC were 5–10 mg. The chosen crystallization temperatures were 73, 83, 93, 101, and  $113 \text{ }^\circ\text{C}$ , respectively, which were the same as those used for the synchrotron X-ray experiments. The subsequent melting scan was measured at a heating rate of  $2 \text{ }^\circ\text{C/min}$ . For comparison, a heating rate of  $10 \text{ }^\circ\text{C/min}$  was also used in DSC measurements.

The sPP film after isothermal crystallization at  $100 \text{ }^\circ\text{C}$  (3 h) was quenched to room temperature and microtomed for TEM observation. TEM specimens were cryofaced at  $-30 \text{ }^\circ\text{C}$  to produce a deformation-free surface with a glass knife and a cryogenic ultramicrotome (Reichert Ultracut E w/FC4D cryostage). A  $\text{RuO}_4$  staining solution was prepared by the addition of 1 mL of a  $\text{NaOCl}$  aqueous solution (10% mass fraction; Aldrich) to 0.02 g of  $\text{RuCl}_3 \cdot n\text{H}_2\text{O}$  in a 5-mL vial, good mixing, and immediate capping. The cryogenically sectioned sample was suspended from the inside of the cap in the vial containing 1 mL of the  $\text{RuO}_4$  solution for 7 h. The samples were then removed from the vial and allowed to degas in a hood for several more hours. Ultrathin-sectioned films (ca. 700–750  $\text{\AA}$  thick) were cut at ambient temperature with a diamond knife and collected in a water floatation bath. Sectioned films were collected onto 200-mesh carbon-coated TEM grids. Images were acquired with a JEOL 2000FX TEM (at 160 kV) and a Gatan MSC-794 CCD.

## RESULTS AND DISCUSSION

Figure 1 shows typical three-dimensional SAXS and WAXD profiles during the isothermal crystallization of sPP at  $101 \text{ }^\circ\text{C}$  and the subsequent melting. In the initial crystallization stages [Fig. 1(a)], the first several SAXS profiles exhibit a sharp monotonous decrease in intensity near the beam-stop position. This low-angle diffuse scattering upturn is frequently observed during time-resolved SAXS measurements of crystallization or melting in polymers and is particularly pronounced either at the beginning of crystallization or at the end of melting. During the induction period of crystallization, there is a gradual increase in the intensity of the low-angle scattering upturn. A scattering maximum at a higher value

of the scattering vector  $q$  ( $=4\pi/\lambda \sin \theta$ , where  $\lambda$  is the wavelength and  $2\theta$  is the scattering angle) also emerges. In the late stages of isothermal crystallization, the SAXS peak becomes well developed and constant, and the intensity of the low-angle upturn remains unchanged. The SAXS peak can be attributed to the lamellar structure in spherulites, which have been verified by TEM observation of the sPP sample isothermally crystallized at  $100 \text{ }^\circ\text{C}$  for 3 h. [Note that there is a small bump ( $q \approx 0.077 \text{ \AA}^{-1}$ ) seen in all SAXS profiles that is due to the physical defect of the detector. This defect was corrected for the data analysis, which did not affect the final SAXS results.] In the WAXD data [Fig. 1(b)], the initial profiles show a broad amorphous peak. The evolution of the orthorhombic crystal structure can be followed by the appearance of {200}, {010}, and {111} reflections, which are marked in Figure 1(b). This orthorhombic structure in sPP is a limit-disordered form I structure, with typical unit cell dimensions of  $a = 14.5 \text{ \AA}$ ,  $b = 5.6 \text{ \AA}$ , and  $c = 7.4 \text{ \AA}$ , that has been reported in melt-crystallized samples with poor syndiospecificity.<sup>6,21,22</sup> Our results are consistent with the previous reports. During subsequent heating from 101 to  $150 \text{ }^\circ\text{C}$  at a  $2 \text{ }^\circ\text{C/min}$  rate [Fig. 1(c)], the SAXS peak shifts to lower  $q$  values, indicating an increase in the long spacing. Eventually, the distinct SAXS peak changes into a scattering shoulder at higher temperatures and completely disappears near the melting point. There is a significant increase in the intensity of the diffuse scattering upturn during heating. A maximum diffuse intensity profile is seen right before final melting takes place [as seen in Fig. 1(d)]. The strong diffuse scattering upturn at low angles is probably due to the disordered structures formed in the heterogeneous melt. The mean size of these disordered structures (several hundred angstroms) is larger than the lamellar spacing of sPP but is still within the detection range of SAXS. Similar observations of the low-angle scattering upturn have been made in semimiscible semicrystalline/amorphous blends [iPP/atactic polypropylene (aPP)], which have been attributed to the morphology containing the aPP-enriched domains excluded from the iPP lamellar microstructures.<sup>4</sup> This observation is made from a single-component polymer system (sPP), which is not due to the phase separation; rather, it reflects the heterogeneous nature of crystal microstructures formed during crystallization and melting. The corresponding WAXD profiles during heating show gradual decreases in

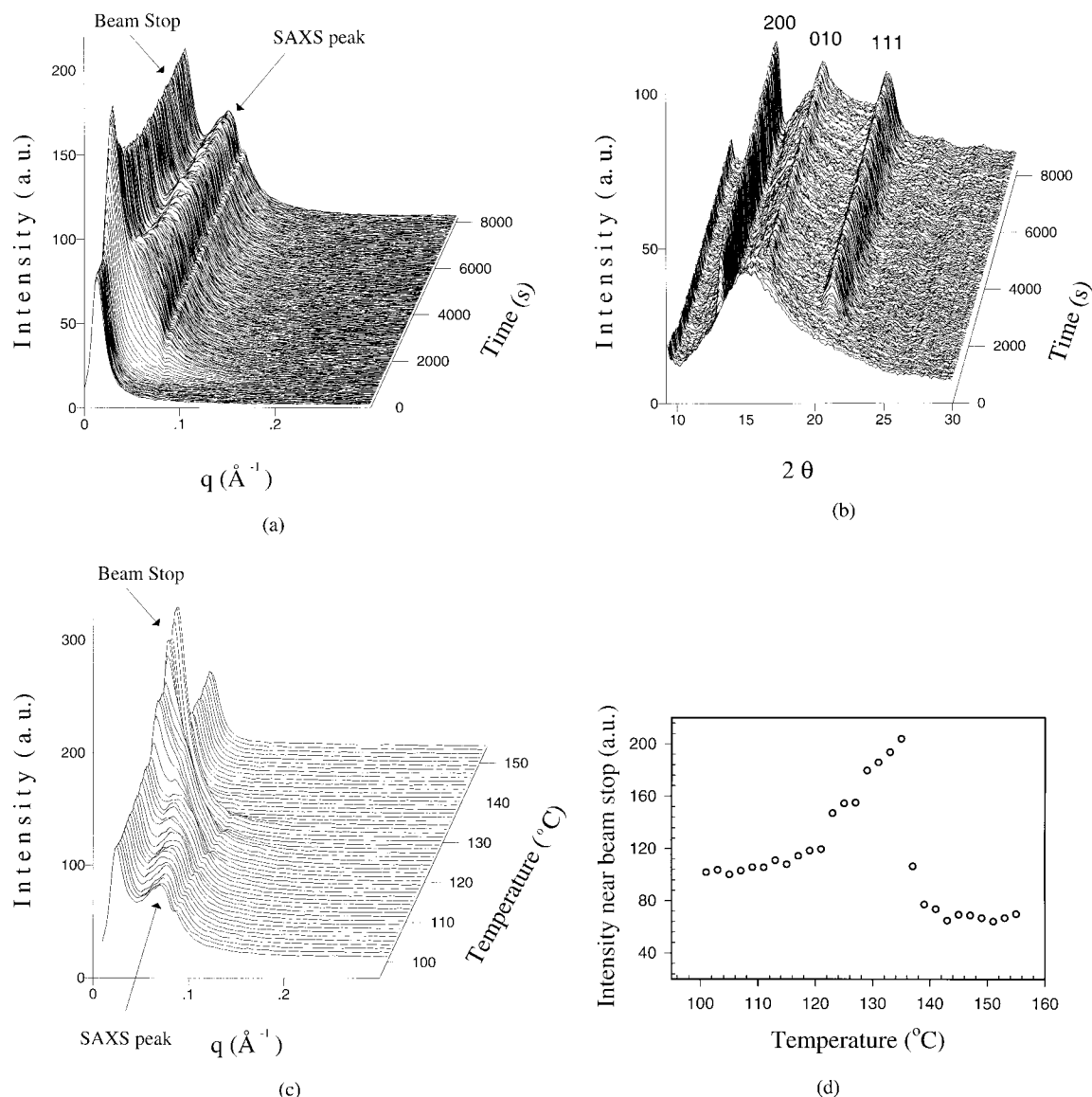


**Figure 1.** Time-resolved (a) SAXS and (b) WAXD patterns during the isothermal crystallization of sPP at 101  $^{\circ}\text{C}$  and (c) SAXS patterns and (d) the intensity near the beam-stop position during subsequent melting at a heating rate of 2  $^{\circ}\text{C}/\text{min}$ .

the intensities of crystal reflections. During careful examinations, we find that the changes in SAXS and WAXD profiles during isothermal crystallization and melting show almost identical trends.

For time-resolved SAXS profiles in semicrystalline polymers, the procedures for analyzing morphological parameters have been well documented.<sup>23–25</sup> The procedures usually involve the use of the correlation function and interference distribution function to extract parameters such as the scattering invariant ( $Q$ ), the long period ( $L$ ), and two thicknesses of the constituent phases

( $l_1$  and  $l_2$ , the crystal and amorphous thicknesses). The assignment of the value representing the crystal thickness has to be carefully justified by a comparison of the SAXS and WAXD results with other independent measurements such as DSC or TEM.<sup>25–29</sup> In this work, the assignment of the crystal lamellar thickness ( $l_c$ ) from the SAXS analysis has been based on TEM observations, which are discussed later.

From the WAXD profile, the peak positions, peak heights, peak widths, and integrated intensities of all crystal reflections and the amorphous background have been extracted with a custom



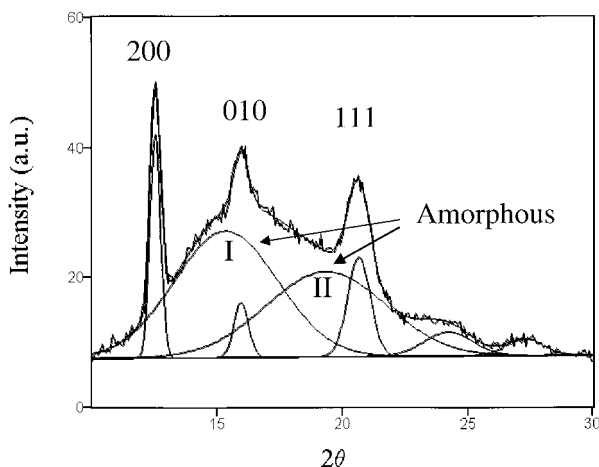


**Figure 2.** Peak deconvolution of the WAXD profile of sPP at 101 °C for 8100 s.

code capable of deconvoluting the time-resolved spectra. Two Gaussian peaks (located at  $2\theta$  values of ca. 15 and 19°) riding on a constant-valued baseline were used to fit the amorphous background (the WAXD pattern from the amorphous melt was used for this purpose). The amorphous background cannot be efficiently described by a single Gaussian peak. All crystal reflection peaks were also fitted with Gaussian functions. By dividing the total intensities of the crystalline reflections ( $I_c$ ) to the overall diffraction intensity ( $I_{\text{total}}$ ), we obtained a measure of the apparent mass fraction of the crystalline phase ( $X_c$ ) in the sample. Because of the possible defects in the crystal lattice as well as thermal disordering at high temperatures, the measured value of  $I_c$  may be lower than the true value. We note that with this deconvolution method, the sample has been assumed to possess an ideal two-phase structure (crystalline and amorphous), which is the criterion for defining the term *crystallinity*. Because the crystal reflection signals are extremely weak during the early stages of crystallization, the determination of the crystallinity is stopped when the crystal reflection {200} cannot be identified. Figure 2 illustrates the typical WAXD deconvolution results for sPP isothermally crystallized at 101 °C for 8100 s. From the peak positions and peak widths of {200} and {010}, the orthorhombic unit cell parameters  $a$  and  $b$  and the lateral crystal sizes  $L_{200}$  and  $L_{010}$  (by the Scherrer equation) can also be calculated.<sup>30</sup>

Figure 3 shows typical time-evolution profiles of morphological parameters extracted from SAXS [ $L$ ,  $l_c$ ,  $l_a$  (interlayer amorphous thickness),

and  $Q$ ] and WAXD [ $X_c$  (apparent mass crystallinity),  $a$  and  $b$ , and  $L_{200}$  and  $L_{010}$ ] for sPP during isothermal crystallization at 101 °C. Figures 4–7 summarize the changes in the morphological parameters extracted from SAXS and WAXD for sPP during subsequent melting from different isothermal crystallization temperatures. For comparison, DSC heating scans with the same heating rate (2 °C/min) are also included. The first derivative curve of  $Q$  ( $dQ/dT$ ) is plotted for comparison with the DSC heating curve. Several distinct features observed in Figures 3–7 can be summarized as follows.

First, the primary isothermal crystallization period can be characterized as the time period of  $t_{c1} < t < t_{c2}$ , where  $t_{c1}$  represents the onset time when  $Q$  and  $X_c$  begin to increase and  $t_{c2}$  represents the onset time when the increases in  $Q$  and  $X_c$  become significantly retarded. During this period, the SAXS patterns show only a weak scattering shoulder, and the morphological parameters of  $L$ ,  $l_c$ , and  $l_a$  cannot be calculated from the correlation function with good confidence. During the secondary crystallization period ( $t > t_{c2}$ ),  $L$  and  $l_c$  (assigned as the larger value of  $l_1$ , which is discussed later) decrease with time. The decreasing values in  $l_c$  and  $L$  can be attributed to the formation of secondary (thinner) lamellae between the primary (thicker) lamellar stacks (this is because  $l_a$  remains almost constant during crystallization).<sup>24,25</sup> The rate of decrease is slower at lower crystallization temperatures because of the reduced chain mobility. The smaller value of the thickness ( $l_2$ ) from the SAXS measurement was assigned as the crystal thickness by Strobl and coworkers,<sup>31,32</sup> who used interface distribution function analysis. The different assignments of  $l_1$  and  $l_2$  have led to very different physical interpretations of the crystallization behavior.

Second, both WAXD  $X_c$  and SAXS  $Q$  show similar trends of rapid increases in value during primary crystallization. Afterward, a continuous increase in  $X_c$  and an almost constant value of  $Q$  are observed during secondary crystallization.

Third, because of the very weak crystal reflection peaks in WAXD during primary crystallization, the unit cell dimensions and lateral crystal sizes cannot be calculated. During secondary crystallization,  $a$  and  $b$  decrease very slightly with time at higher crystallization temperatures (93 and 101 °C) but decrease significantly at lower crystallization temperatures (73 and 83 °C). This can be attributed to the defective crystal structure formed at lower crystallization tempera-

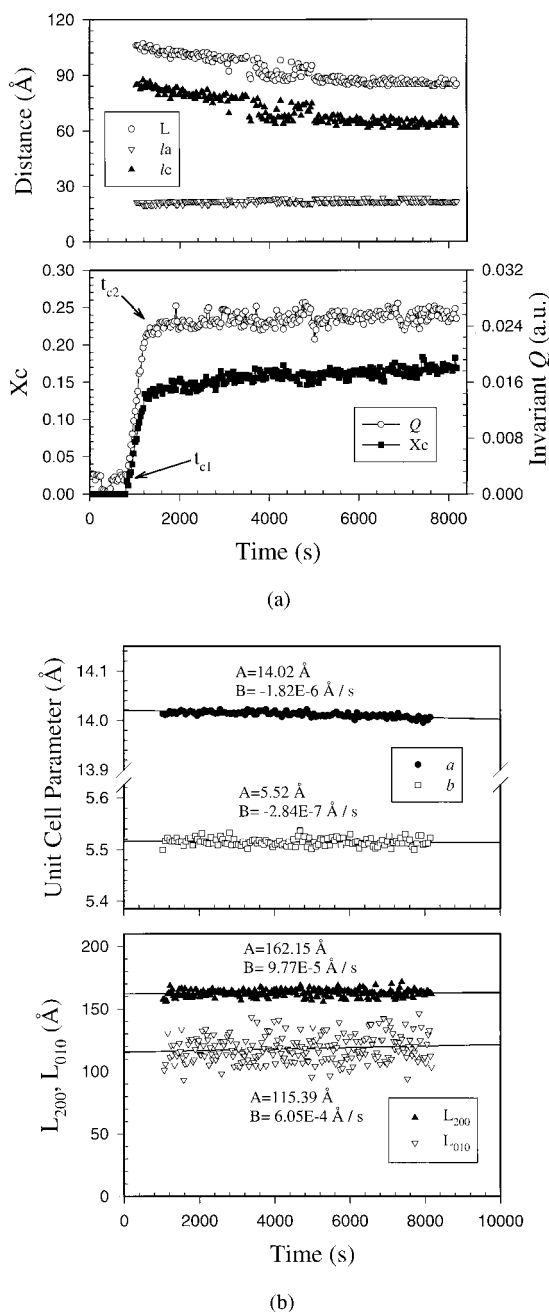


**Figure 3.** (a) Time evolution of  $L$ ,  $l_c$ , and  $l_a$  (top) and SAXS  $Q$  and WAXD  $X_c$  (bottom) during the isothermal crystallization of sPP at 101 °C and (b) time evolution of  $a$  and  $b$  (top) and  $L_{200}$  and  $L_{010}$  (bottom) from WAXD profiles during the isothermal crystallization of sPP at 101 °C (the solid lines are obtained by linear fitting). The relative standard deviations for the fits of  $a$ ,  $b$ ,  $L_{200}$ , and  $L_{010}$  are less than 1, 1, 1, and 2%, respectively, and are suitable for the data in Figures 4–8.

tures, which is then driven to crystal perfection by long-time annealing. The contraction of the unit cell dimensions during isothermal crystalli-

zation has also been observed in other polymers.<sup>33–35</sup>  $L_{200}$  (162 Å) and  $L_{010}$  (108 Å), however, remain about constant during secondary crystallization.

Fourth, when isothermally crystallized sPP samples are heated at a 2 °C/min rate immediately after crystallization, the changes in the morphological parameters ( $Q$ ,  $X_c$ ,  $L$ , and  $l_c$ ) appear to follow a two-stage process. These two stages are consistent with the multiple melting endothermic peaks observed in the DSC scan. The first derivative curve of  $Q$  ( $dQ/dT$ ) clearly illustrates this correlation [Figs. 4(a)–7(a)]. The  $dQ/dT$  curve also exhibits two primary transition peaks. The peak temperatures appear to occur at higher values than those in DSC. The difference in the peak temperatures between  $dQ/dT$  and DSC is due to the different nature of the technique; that is, DSC detects the heat flow, and SAXS detects the density contrast change. It is reasonable to argue that the contrast change may lag behind the heat flow because the polymer chains require some time to reorganize themselves after melting.

The two-stage process is also evident in the changes in  $L$  and  $l_c$  during melting. Both  $L$  and  $l_c$  show notable increases immediately after the first melting endotherm ( $T_{m1}$ ). The increases suggest that a significant portion of the lamellar structures generated by isothermal crystallization become molten during the first melting process. The second melting peak is related to the recrystallization and melting process. The recrystallization process coincides with the appearance of a hump in the  $L$  profile [marked by an arrow at the highest temperature in Figs. 4(a)–7(a)]. Larger (thicker) lamellae are formed during the second stage because of higher crystallization temperatures (or lower degrees of undercooling).

Fifth, the step-change behavior in unit cell parameters and lateral crystal sizes during heating is seen in Figures 4(b)–7(b). For example, Figure 4(b) (samples isothermally crystallized at 101 °C) shows a slight increase in  $a$  before 127 °C and a decrease afterward. In contrast,  $a$  remains about constant before 120 °C and decreases afterward [Figs. 5(b)–7(b), with crystallization temperatures of 73, 83, and 93 °C, respectively]. The linear extrapolation of each step is listed alongside the data fit. The aforementioned behavior can be explained as follows. At high temperatures (>101 °C), sPP can crystallize into a relatively perfect form, enabling the effect of thermal expansion (an increase in  $a$ ) to be dominant upon subsequent heating. At low crystallization temperatures (<93 °C), sPP crystallizes into a more defective form

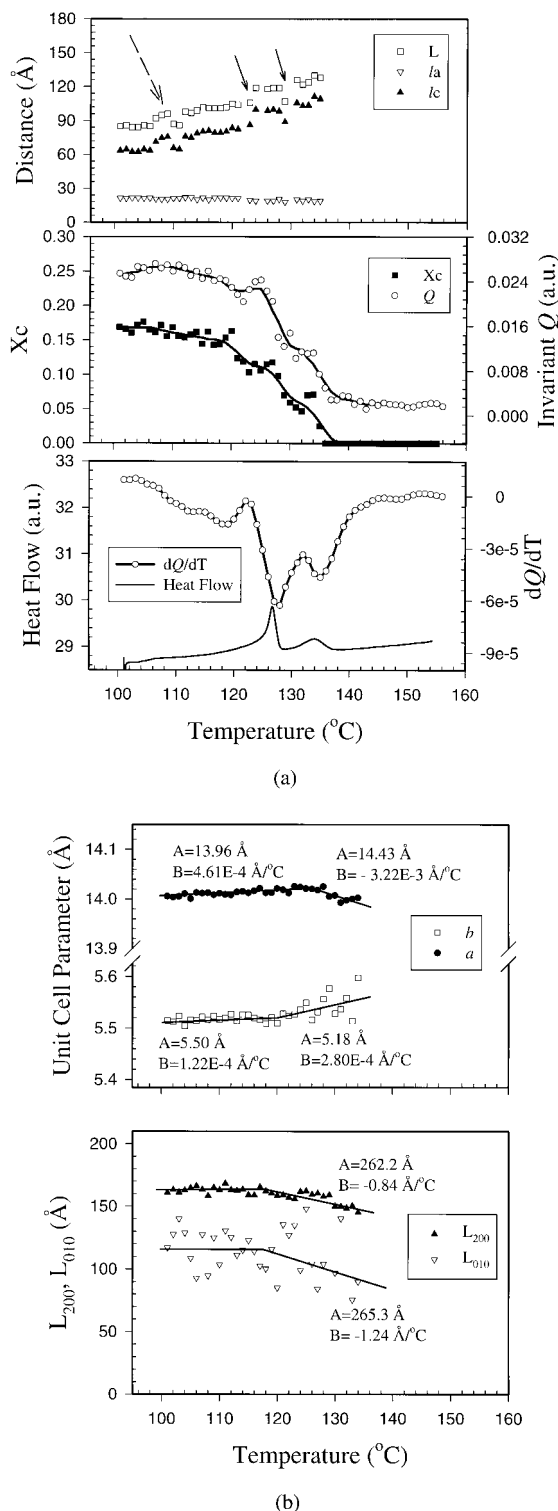


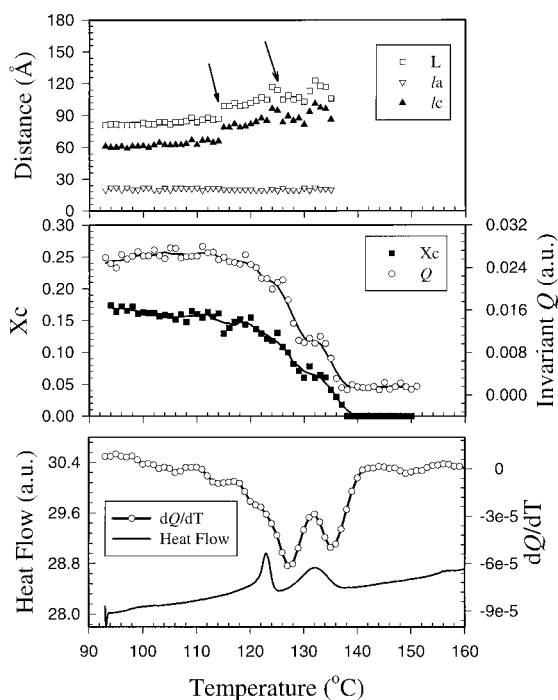
**Figure 4.** (a) Time evolution of SAXS  $L$ ,  $l_c$ , and  $l_a$  (top), SAXS  $Q$  and WAXD  $X_c$  (middle; the solid curves are obtained by five-point, adjacent, smooth averaging), and DSC heat flow and  $dQ/dT$  (bottom) during the subsequent melting of sPP from 101 °C and (b) time evolution of  $a$  and  $b$  (top) and  $L_{200}$  and  $L_{010}$  (bottom) from WAXD profiles during the melting process of sPP from 101 °C (the solid lines are obtained by linear

such that competition between thermal expansion (an increase in  $a$ ) and crystal perfection (a decrease in  $a$ ) takes place, resulting in a constant value of  $a$ . Comparing the changes in  $a$  and the DSC results, we find that  $a$  increases or remains constant in the region before the second endotherm. During the second endothermic transition, a notable decrease in  $a$  is seen that is related to the process of recrystallization.

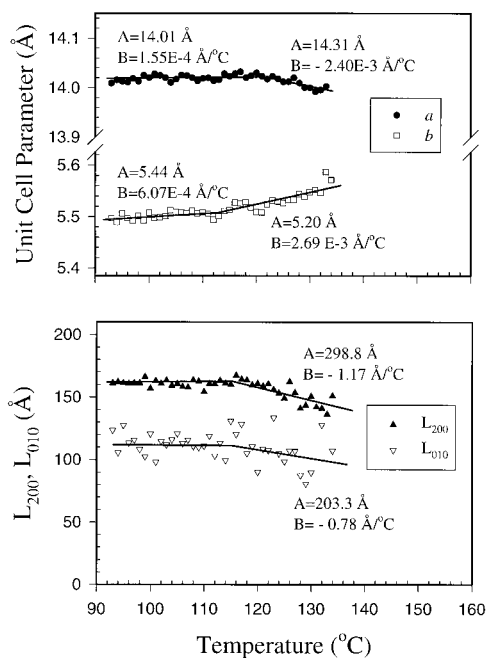
The evolution of  $b$  also indicates a step-change behavior but in a different fashion.  $b$  remains constant or increases slightly below a different onset temperature [120 °C in Fig. 4(b), 113 °C in Fig. 5(b), and 110 °C in Fig. 6(b)] and exhibits an increase afterward. In Figure 7(b), where no clear step-change behavior is seen,  $b$  increases almost continuously during heating from the crystallization temperature (73 °C). As mentioned earlier, the change in the unit cell parameters is a result of two opposite effects: (1) contraction due to crystal perfection and (2) expansion due to thermal vibration. The effect of thermal expansion on  $b$  appears to be much more pronounced than that on  $a$  (as seen by the large increase in  $b$  at low temperatures). This is consistent with the report by Lovinger et al.<sup>36</sup> that the thermal expansion coefficient is greater along the  $b$  axis than along the  $a$  axis in sPP. Molecular simulations of the temperature dependence of sPP crystals carried out by Lacks and Rutledge<sup>37</sup> suggested that its thermal expansion anisotropy arises from the larger thermal stress, lower chain stiffness, and a smaller Poisson coefficient along the  $b$  axis. The average onset temperature (ca. 110–120 °C), where the step-change in the unit cell parameters ( $a$  and  $b$ ) is seen, somewhat coincides with the regime II–III transition temperature (ca. 110 °C) during the crystallization of sPP<sup>38</sup> as well as the melting temperature of the first endotherm.

In addition to the unit cell parameters,  $L_{200}$  and  $L_{010}$  also exhibit a step-change behavior. In Figures 4(b)–7(b), both  $L_{200}$  and  $L_{010}$  remain about constant before the onset temperature (ca. 110–120 °C, similar to the values for  $a$  and  $b$ ) and decrease afterward. This behavior was also reported by Cheng et al.<sup>12</sup> The decrease in crystal sizes after the first endotherm suggests that more perfect crystals are formed during the recrystallization process.

fitting within an appropriate temperature range; the constants  $A$  and  $B$  represent the intercept and slope of the linear fitting, respectively].



(a)



(b)

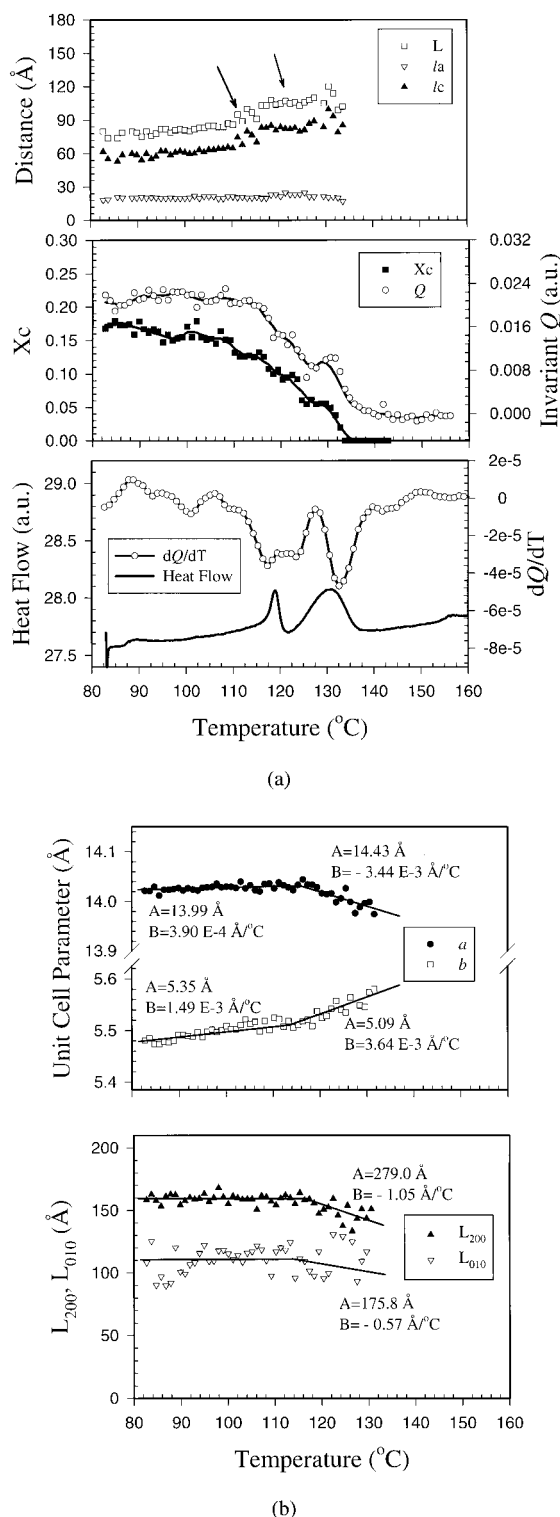
**Figure 5.** (a) Time evolution of SAXS  $L$ ,  $l_c$ , and  $l_a$  (top), SAXS  $Q$  and WAXD  $X_c$  (middle; the solid curves are obtained by five-point, adjacent, smooth averaging), and DSC heat flow and  $dQ/dT$  (bottom) during the subsequent melting of sPP from 93 °C and (b) time evolution of  $a$  and  $b$  (top) and  $L_{200}$  and  $L_{010}$  (bottom) from WAXD profiles during the melting process of sPP from 93 °C (the solid lines are obtained by linear fitting

Figure 8(a) summarizes the plateau long period ( $L^*$ ), plateau lamellar thickness ( $l_c^*$ ), and plateau amorphous thickness ( $l_a^*$ ) of sPP after isothermal crystallization at long times. Both  $L^*$  and  $l_c^*$  increase with crystallization temperature, whereas the increase in  $l_a^*$  is only minor. This phenomenon is similar to the recent findings in several semicrystalline polymers, including poly(butylene terephthalate) (PBT),<sup>25</sup> poly(ethylene terephthalate) (PET),<sup>26</sup> nylon-66,<sup>27</sup> poly(glycolide-co-lactide) (PGA-co-PLA),<sup>29</sup> and iPP.<sup>30</sup> The value of  $L^*$  in Figure 8(a) is smaller than the value obtained from a different sPP sample (with a similar molecular weight) under the same crystallization conditions in ref. 5. The difference in  $L^*$  may be due to the poor stereospecificity of the sPP sample in this study, which is evident from the lower heat of fusion ( $\Delta H$ ) and lower melting temperature ( $T_m$ ) with respect to those of the higher stereospecific sample ( $\Delta H \approx 45$  vs 60 J/g and  $T_m \approx 145$  vs 150 °C).

The increase in  $l_c^*$  at higher temperatures can be rationalized by the thermodynamic factors driven by the higher chain mobility and the greater ability of polymer segments to disentangle. We have adopted the approach of Spruiell et al.<sup>22</sup> to analyze these results. Based on their method, the temperature-dependent lamellar thickness can be fitted by a simple equation,  $l_c^* = D_1/\Delta T + D_2$ , where  $D_1$  and  $D_2$  are constants and  $\Delta T$  ( $T_m^0 - T_c$ , where  $T_m^0$  is the equilibrium melting temperature and  $T_c$  is the crystallization temperature) is the degree of undercooling. As discussed in their article, two different values of  $T_m^0$  for sPP were estimated: (1) 166.3 °C from the Gibbs–Thomson extrapolation method and (2) 184.7 °C from the nonlinear Hoffman–Weeks extrapolation method. We have also used these two estimated  $T_m^0$  values to analyze the SAXS results (the sample in our study appears to be similar to the sample in the study of Spruiell et al.). We obtained the following results. The thick solid line shown in Figure 8(a) ( $l_c^*$  and  $L^*$  are measured in angstroms, and  $T_c$  is measured in degrees Celsius) represents the fitted curve with  $T_m^0 = 166.3$  °C, which yields  $D_1 = 3970.7 \text{ Å °C}$ ,  $D_2 = 7.5 \text{ Å}$ , and  $R = 0.975$ , where  $R$  is the correlation coefficient of the fit. When  $T_m^0 = 184.7$  °C is used, the

within an appropriate temperature range; the constants  $A$  and  $B$  represent the intercept and slope of the linear fitting, respectively].





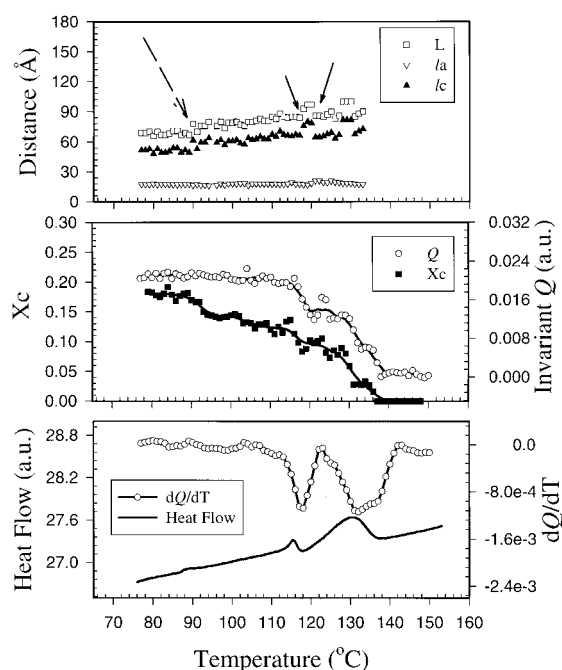
**Figure 6.** (a) Time evolution of SAXS  $L$ ,  $l_c$ , and  $l_a$  (top), SAXS  $Q$  and WAXD  $X_c$  (middle; the solid curves are obtained by five-point, adjacent, smooth averaging), and DSC heat flow and  $dQ/dT$  (bottom) during the subsequent melting of sPP from 83 °C and (b) time evolution of  $a$  and  $b$  (top) and  $L_{200}$  and  $L_{010}$  (bottom) from WAXD profiles during the melting process of sPP

fitted curve gives  $D_1 = 6381.8 \text{ Å °C}$ ,  $D_2 = -7.5 \text{ Å}$ , and  $R = 0.971$ . Both fits show good  $R$  values. However, when  $T_m^\circ = 184.7 \text{ °C}$  is used,  $D_2$  becomes negative, which has no physical meaning. Consequently, the  $T_m^\circ = 166.3 \text{ °C}$  is more reasonable according to this study.

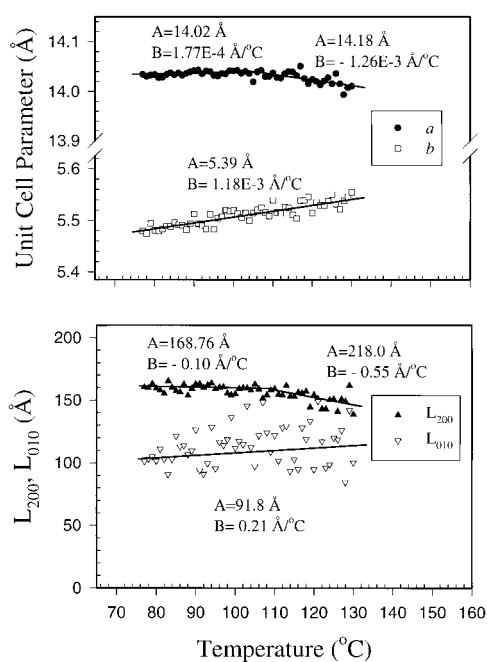
The determination of  $l_c^*$  in this article is directly calculated from the correlation function, whereas the lamellar thickness in Spruiell et al.'s<sup>22</sup> study was calculated as the product of  $L$  and WAXD  $X_c$ .<sup>22</sup> The difference between these two calculations is quite significant because the sPP sample with poor syndiospecificity has a relatively low crystallinity. The true crystal thickness can be significantly underestimated in samples of low crystallinity with the latter approach.<sup>24</sup> The justification of the crystal thickness determination is provided later.

To grasp the issue of crystallinity, we have carried out the following analysis. In Figure 8(b), we compare  $X_c$  calculated from DSC and  $X_c$  from WAXD at different temperatures. The heat of fusion values for sPP with 100% crystallinity ( $\Delta H_f^\circ$ ) given in the literature vary between 6.9 and 8.7 kJ mol<sup>-1</sup> (based on per propylene units C<sub>3</sub>H<sub>6</sub>).<sup>39,40</sup> Both values (6.9 and 8.7 kJ mol<sup>-1</sup>) were used in this study to calculate DSC  $X_c$  [Fig. 8(b)], and the results are indicated by the different symbols. WAXD  $X_c$  shows a very slight increase with  $T_c$ , which is normally observed in polymer crystallization. In contrast, DSC  $X_c$  shows a notable decrease with  $T_c$ . We rationalize the difference as follows. WAXD  $X_c$  directly measures the relative content of the crystal phase formed during the isothermal crystallization process, whereas DSC  $X_c$  detects the total enthalpy change, which is more sensitive to any process that will induce heat flow. We feel, at a 2 °C/min heating rate, the system has ample time to recrystallize at lower temperatures. As a result, DSC  $X_c$  shows a slight decrease with  $T_c$ , as the total enthalpy change is reduced. The smaller value of  $X_c$  from DSC may also be due to the difficulty in properly determining the background in the DSC thermogram. Another reason may be that the  $\Delta H_f^\circ$  values quoted in this article are probably at the high end of the published range (values as low as

from 83 °C (the solid lines are obtained by linear fitting within an appropriate temperature range; the constants  $A$  and  $B$  represent the intercept and slope of the linear fitting, respectively).



(a)



(b)

**Figure 7.** (a) Time evolution of SAXS  $L$ ,  $l_c$ , and  $l_a$  (top), SAXS  $Q$  and WAXD  $X_c$  (middle; the solid curves are obtained by five-point, adjacent, smooth averaging), and DSC heat flow and  $dQ/dT$  (bottom) during the subsequent melting of sPP from 73 °C and (b) time evolution of  $a$  and  $b$  (top) and  $L_{200}$  and  $L_{010}$  (bottom) from WAXD profiles during the melting process of sPP from 73 °C (the solid lines are obtained by linear fitting within an appropriate temperature range; the constants

4.4 kJ mol<sup>-1</sup> have also been reported<sup>2,41</sup>). Because we are mostly interested in the temperature dependence of relative crystallinity in this study, the true value of  $\Delta H_f^0$  is not critical for the analysis.

Figure 9(a) shows the heat flow during isothermal crystallization at 93 and 101 °C, respectively. The times  $t_s$  and  $t_e$  are marked to indicate the start and end times of the exothermic crystallization process at 93 °C. These characteristic times (from DSC) are compared with similar time parameters obtained from SAXS measurements [Fig. 3(a)], as shown in Figure 9(b). The crystallization start and end times exhibit a similar trend of change (exponential-like) with  $T_c$  from these two techniques. The DSC data, however, show a larger range between  $t_s$  and  $t_e$  than SAXS ( $t_{c1}$  and  $t_{c2}$ ), especially at higher  $T_c$ 's. The higher the  $T_c$  is, the larger the discrepancy is between the start and end times. This suggests that nucleation is prolonged at higher temperatures because of large Brownian motions of polymer chains.

Figure 9(c,d) shows DSC heating scans of the samples crystallized at different values of  $T_c$  at 2 and 10 °C/min rates, respectively. These samples were isothermally crystallized under the same conditions used for the X-ray measurements. At the 2 °C/min heating rate, dual endotherms (indicated by I and II) are seen at all  $T_c$ 's. At the 10 °C/min heating rate, dual endotherms are not observed at high  $T_c$ 's. The peak temperature of the lower melting endotherm is represented by  $T_{m1}$ , and the peak temperature of the higher melting endotherm is represented by  $T_{m2}$ . The corresponding enthalpy changes are represented by  $\Delta H_1$  and  $\Delta H_2$ , respectively. Figure 10(a,b) shows the endothermic peak temperature and the corresponding enthalpy change as a function of  $T_c$  measured at the 2 °C/min rate. With the increase in  $T_c$ , both  $T_{m1}$  and  $T_{m2}$  increase, with  $T_{m1}$  showing a much greater rate. In Figure 10(b), when  $T_c$  increases,  $\Delta H_1$  increases,  $\Delta H_2$  decreases, and the total enthalpy change also shows a slight decrease. Comparing this data to the time evolution of the SAXS morphological parameters, we can reasonably conclude that the dual melting peaks can be attributed to the melting of primary lamellae ( $T_{m1}$ ) and the recrystallization-melting pro-

A and B represent the intercept and slope of the linear fitting, respectively].

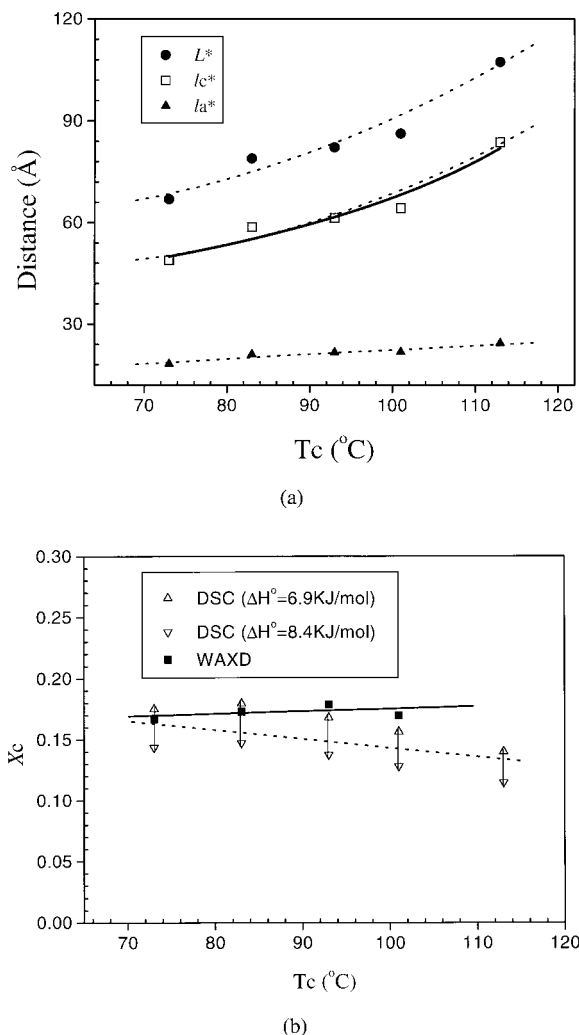


**Figure 8.** (a) SAXS  $L^*$ ,  $l_c^*$ , and  $l_a^*$  (top; the dotted lines are obtained by polynomial fitting, and the thick solid line is fitted with the equation given in the text) and (b) WAXD  $X_c$  and DSC  $X_c$  (bottom) at different temperatures.

cess ( $T_{m2}$ ), respectively. We note that there are two additional minor endotherms located at the very low and very high temperatures. The highest temperature endotherm ( $\approx 156.8$  °C) has a constant peak temperature independent of  $T_c$  and the heating rate. This endothermic peak, occurring beyond the melting range of sPP, is not related to the melting of some impurities in sPP because the peak is also present in the background (empty-pan) scan. The lowest endotherm (marked  $T_{m0}$ ) increases with  $T_c$  as well as the heating rate. At 2 °C/min,  $T_{m0}$  is consistently 5–7 °C higher than  $T_c$  (except at 73 °C, where the difference is 16.6 °C). At 10 °C/min,  $T_{m0}$  is approximately 11 °C higher than  $T_c$ . This low endotherm

is widely known in semicrystalline polymers and is induced by isothermal annealing. The melting of the secondary thinner or small defective lamellae can be attributed to this endotherm; this is consistent with the observation that above this lowest endothermic temperature, there is a visible increase in the long period and lamellar thickness as shown in Figures 4(a) and 7(a) (marked by the dash arrow). The melting behavior of sPP is very similar to that of PET, for which triple melting behavior has also been reported.<sup>26</sup> Recently, studies of isothermal melt- and cold-crystallization kinetics and subsequent melting behavior of sPP by DSC were carried out by Supaphol and Spruiell.<sup>42</sup> Our results and interpretation are quite consistent with theirs.

Because we are dealing with the subject of the time evolution of morphological parameters by SAXS in reciprocal space, it is very important and necessary to first identify the morphology in real space. One of the problems pointed out earlier is that the larger thickness in the two-phase model determined from the SAXS correlation function analysis can be assigned as either  $l_c$  or  $l_a$ ; this needs to be verified by other independent techniques such as TEM. Figure 11 shows selected TEM images of an sPP sample (crystallized at 100 °C for 3 h) that was microtomed and stained. It is very clear that lamellar structures are formed in this fully crystallized sample (although  $X_c$  is only 20% by mass). Two distinct features are seen in these TEM images: (1) the average value of  $l_c$  (indicated by the light regions) is larger than the average value of  $l_a$  (indicated by the dark regions) in the stacks and (2) the lamellar distribution is not completely space-filled because there are large amorphous domains present between the lamellar stacks. The dark regions represent the amorphous phases, as they are stained by  $\text{RuO}_4$ , enhancing the TEM contrast. The average value of  $l_a$  is less than 27 Å, and the average value of  $l_c$  lies between 64 and 82 Å. These results are consistent with the SAXS results shown in Figures 3(a) and 4(a) (crystallized at 101 °C for 138 min). In Figure 3(a), the final average lamellar thickness is approximately 60 Å because of the thinner lamellae formed during secondary crystallization, making the average lamellar thickness smaller than the mean lamellar thickness seen in TEM. As a result, we feel confident that the lamellar thickness in sPP is larger than the product of  $X_c$  (from WAXD) and  $L$  (from SAXS), as the sPP morphology is not space-filled. The TEM result supports our early assertion that the correct

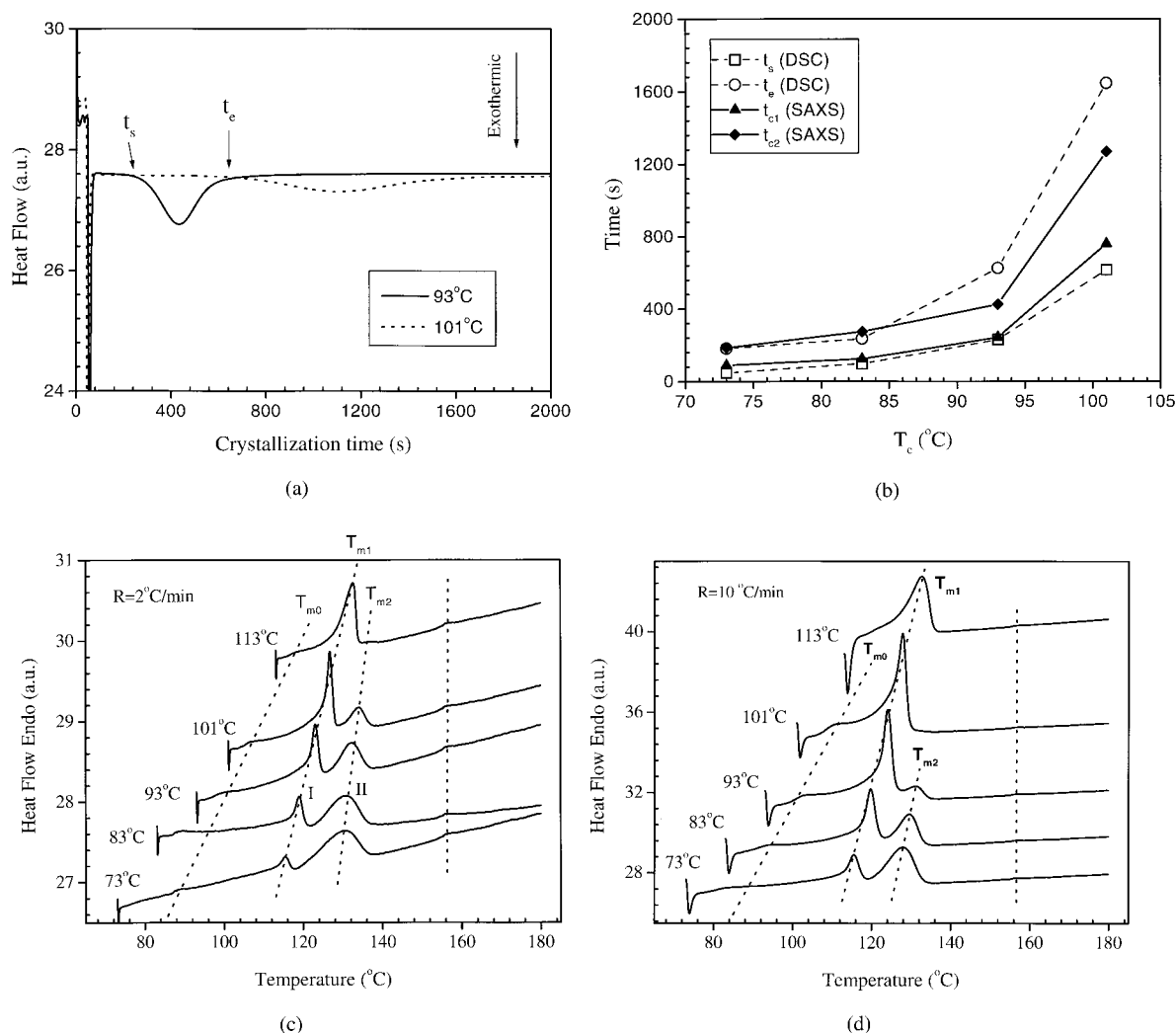


**Figure 9.** (a) Typical crystallization exotherms of sPP during isothermal crystallization at 101 and 93 °C from the melt, (b) characteristic times from DSC and SAXS that illustrate the start and end times for primary crystallization, (c) subsequent melting endotherms of sPP at 2 °C/min after isothermal crystallization at specified temperatures, and (d) subsequent melting endotherms of sPP at 10 °C/min after isothermal crystallization at specified temperatures. The dotted lines in Figure 9 (c,d) indicate the transitions of interest.

value of  $l_c$  is the larger thickness value obtained by the SAXS analysis. This assignment is the opposite of that in recent articles by Strobl and coworkers (sPP),<sup>10,31,32</sup> who used the small value as  $l_c$ . As a result, their explanations for the crystallization and melting behavior in sPP are completely different.

## CONCLUSIONS

Morphological and structural parameters ( $L$ ,  $l_c$ ,  $l_a$ ,  $Q$ ,  $X_c$ ,  $L_{200}$ ,  $L_{010}$ ,  $a$ , and  $b$ ) during the isother-

mal crystallization and subsequent melting of sPP were investigated by simultaneous time-resolved SAXS/WAXD with synchrotron radiation. These parameters were compared with the multiple melting behavior observed by DSC. TEM was also used to reveal the real space information of the crystal lamellae. The SAXS results indicate that the decreases in  $L$  and  $l_c$  are related to the formation of thinner secondary crystal lamellae between the primary lamellar stacks during isothermal crystallization. However, the decreases in  $a$  and  $b$  (from WAXD) during crystallization



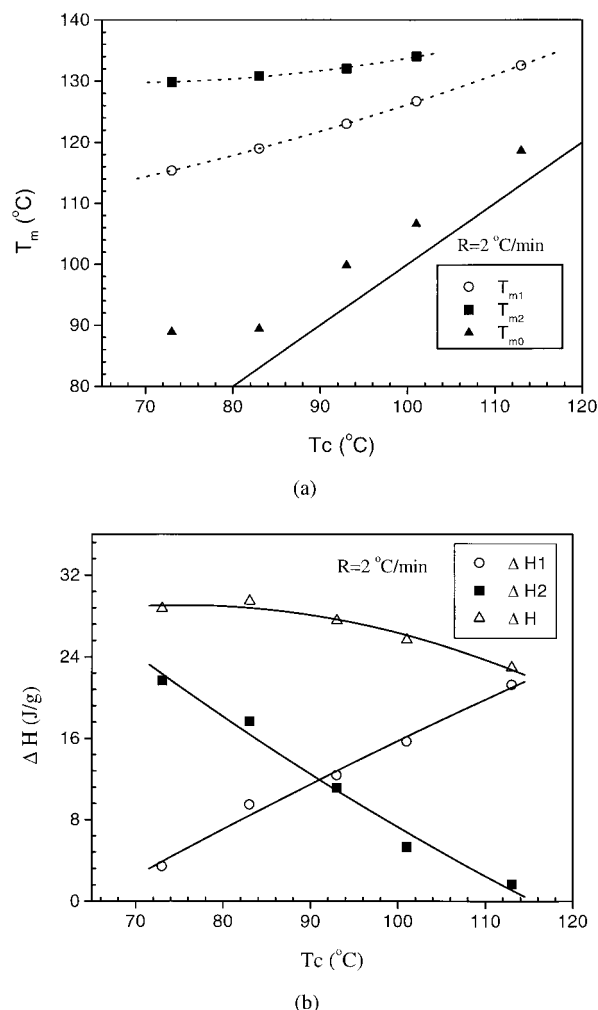


**Figure 10.** Changes in (a) the melting points (the dotted lines through the data are obtained by polynomial fitting, and the solid line represents  $T_m = T_c$ ) and (b) the enthalpies (the lines through the data are obtained by polynomial fitting) during melting (2 °C/min). The relative standard deviations for the melting point and enthalpy are less than 0.5 and 2%, respectively.

can be related to crystal perfection. A clear two-stage melting process was seen in the changes in the morphological parameters ( $Q$ ,  $X_c$ ,  $L$ , and  $l_c$ ) during subsequent melting, and this behavior is consistent with the multiple melting behavior in DSC. The two dominant melting endotherms in DSC can be attributed to the melting of primary lamellae ( $T_{m1}$ ) and the melting of recrystallized lamellae ( $T_{m2}$ ). An additional small endotherm located at the lowest temperature was also detected that might have been due to the melting of the thinner secondary lamellae. TEM of the fully crystallized sPP sample revealed a clear lamellar

morphology, which is consistent with the SAXS results. The average crystal thickness estimated from TEM confirms that the larger thickness ( $l_1$ ) calculated from the correlation function should be assigned as the lamellar thickness.

The authors thank Dr. Dufei Fang, Dr. Lizhi Liu, and Dr. Fengji Yeh (State University of New York at Stony Brook) for providing invaluable support for the synchrotron measurements and Mr. Gary M. Brown

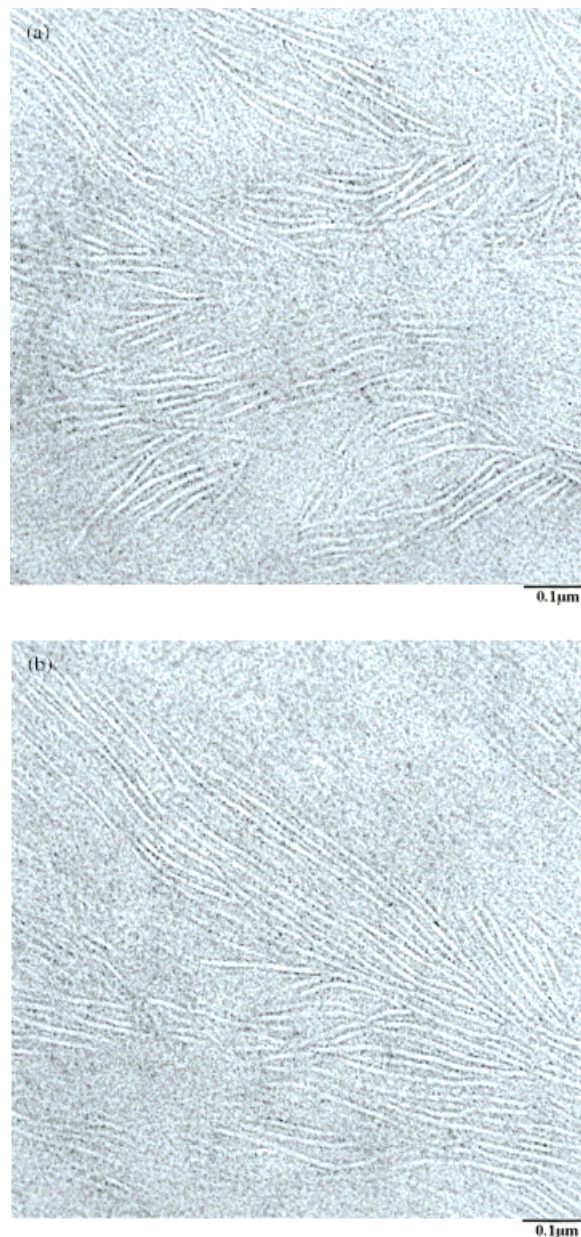


**Figure 11.** Morphology of sPP lamellae crystallized at 100 °C for 3 h as observed by TEM [Fig. 11(a,b) represents different locations in the sample].

(ExxonMobil) for providing the TEM measurements. B. S. Hsiao and Z.-G. Wang acknowledge the financial support of this work through grants from the National Science Foundation (DMR0098104) and the National Institute of Standards and Technology.

## REFERENCES AND NOTES

- Roder, H.; Vogl, O. *Prog Polym Sci* 1999, 24, 1205.
- Phillips, R. A.; Wolkowicz, M. D. In *Polypropylene Handbook*; Moore, E. P., Ed.; Hanser: Munich, 1996.
- Phillips, R. A. *J Polym Sci Part B: Polym Phys* 2000, 38, 1947.
- Wang, Z. G.; Phillips, R. A.; Hsiao, B. S. *J Polym Sci Part B: Polym Phys* 2000, 38, 2580.
- Wang, Z. G.; Phillips, R. A.; Hsiao, B. S. *J Polym Sci Part B: Polym Phys* 2001, 39, 1876.
- Phillips, R. A.; Jones, R. L. *Macromol Chem Phys* 1999, 200, 1912.
- Thomann, R.; Wang, C.; Kressler, J.; Jungling, S.; Mulhaupt, R. *Polymer* 1995, 36, 3795.
- Haylock, J. C.; Phillips, R. A.; Wolkowicz, M. D. In *Metallocene Based Polyolefins: Preparation, Properties and Technology*; Scheirs, J.; Kaminsky, W., Eds.; Wiley: Chichester, England, 2000; Vol. 2, pp 333–363.
- Shiomura, T.; Uchikawa, N.; Asanuma, T.; Sugimoto, R.; Fujio, I.; Kimura, S.; Harima, S.; Akiyama, M.; Kohno, M.; Inoue, N. In *Metallocene Based Polyolefins: Preparation, Properties and Technology*; Scheirs, J.; Kaminsky, W., Eds.; Wiley: Chichester, England, 1999; Vol. 1, pp 437–466.
- Schmidtke, J.; Strobl, G.; Thurn-Albrecht, T. *Macromolecules* 1997, 30, 5804.
- Rodriguez-Arnold, J.; Bu, Z. Z.; Cheng, S. Z. D.; Hsieh, E. T.; Johnson, T. W.; Geerts, R. G.; Palackal, S. J.; Hawley, G. R.; Welch, M. B. *Polymer* 1994, 35, 5194.
- Rodriguez-Arnold, J.; Zhang, A.; Cheng, S. Z. D.; Lovinger, A. J.; Hsieh, E. T.; Chu, P.; Johnson, T. W.; Honnell, K. G.; Geerts, R. G.; Palackal, S. J.; Hawley, G. R.; Welch, M. B. *Polymer* 1994, 35, 1884.
- Lovinger, A. J.; Davis, D. D.; Lotz, B. *Macromolecules* 1991, 24, 552.
- Kressler, J. In *Polypropylene an A–Z Reference*; Karger-Kocsis, J., Ed.; Kluwer Academic: Dordrecht, 1999; p 142.
- Lovinger, A. J.; Lotz, B.; Davis, D. D.; Padden, F. J. *Macromolecules* 1993, 26, 3494.
- Zhou, W.; Cheng, S. Z. D.; Putthanarat, S.; Eby, R. K.; Reneker, D. H.; Lotz, B.; Magonov, S.; Hsieh, E. T.; Geerts, R. G.; Palackal, S. J.; Hawley, G. R.; Welch, R. B. *Macromolecules*, 2000, 33, 6861.
- Ohira, Y.; Horii, F.; Nakaoki, T. *Macromolecules* 2000, 33, 5566.
- According to ISO Standard 31-8, the term *molecular weight* has been replaced by *relative molecular mass* ( $M_r$ ). Thus, if this nomenclature and notation were followed in this article, we would write  $M_{r,n}$  instead of the historically conventional  $M_n$  for the number-average molecular weight, with similar changes for  $M_w$  and  $M_z$ , and it would be called the *number-average relative molecular mass*. The conventional notation, rather than the ISO notation, has been used in this article.
- Certain equipment and instruments or materials are identified in this article for adequate specification of the experimental details. Such identification does not imply recommendations by the National Institute of Standards and Technology, nor does it imply that the materials are necessarily the best available for the purpose.
- Song, H. H.; Wu, D. Q.; Chu, B.; Satkowski, M.; Stein, R. S.; Phillips, J. C. *Macromolecules* 1990, 23, 2380.
- De Rosa, C.; Talarico, G.; Caporaso, L.; Auriemma, F.; Galimberti, M.; Fusco, O. *Macromolecules* 1998, 31, 9109.
- Supaphol, P.; Spruiell, J. E.; Lin, J. S. *Polym Int* 2000, 49, 1473.
- Strobl, G. R.; Schnieder, M. J. *J Polym Sci Polym Phys Ed* 1981, 19, 1361.
- Verma, R.; Marand, H.; Hsiao, B. S. *Macromolecules* 1996, 29, 7767.
- Hsiao, B. S.; Wang, Z. G.; Yeh, R.; Gao, Y.; Sheth, K. C. *Polymer* 1999, 40, 3515.
- Wang, Z. G.; Hsiao, B. S.; Sauer, B. B.; Kampert, W. G. *Polymer* 1999, 40, 4615.
- Wang, Z. G.; Hsiao, B. S.; Murthy, N. S. *J Appl Crystallogr* 2000, 33, 690.
- Wang, Z. G.; Hsiao, B. S.; Fu, B. X.; Liu, L.; Yeh, F.; Sauer, B. B.; Chang, H.; Schultz, J. M. *Polymer* 2000, 41, 1791.
- Wang, Z. G.; Hsiao, B. S.; Zong, X. H.; Yeh, F.; Zhou, J. J.; Dormier, E.; Jamiolkowski, D. D. *Polymer* 2000, 41, 621.
- Wang, Z. G.; Hsiao, B. S.; Sirota, E. B.; Agarwal, P.; Srinivas, S. *Macromolecules* 2000, 33, 978.
- Heck, B.; Hugel, T.; Lijima, M.; Strobl, G. *Polymer* 2000, 41, 8839.
- Hauser, G.; Schmidtke, J.; Strobl, G.; Thurn-Albrecht, T. *Am Chem Soc Symp Ser* 2000, 739, 140.
- Wang, Z. G.; Hsiao, B. S.; Lopez, J.; Armistead, J. P. *J Polym Res* 1999, 6, 167.
- Fougnies, C.; Damman, P.; Villers, D.; Dosiere, M.; Koch, M. H. J. *Macromolecules* 1997, 30, 1385.
- Fougnies, C.; Damman, P.; Dosiere, M.; Koch, M. H. J. *Macromolecules* 1997, 30, 1392.
- Lovinger, A. J.; Lotz, B.; Davis, D. D.; Schumacher, M. *Macromolecules* 1994, 27, 6603.
- Lacks, D. J.; Rutledge, G. *Macromolecules* 1995, 28, 5789.
- Supaphol, P.; Spruiell, J. E. *Polymer* 2000, 41, 1205.
- Balbontin, G.; Dainelli, D.; Galimberti, M.; Paganetto, G. *Makromol Chem* 1992, 193, 693.
- Haftka, S.; Konnecke, K. *J Macromol Sci Phys* 1991, 30, 319.
- Supaphol, P. *J Appl Polym Sci* 2001, 79, 1603.
- Supaphol, P.; Spruiell, J. E. *Polymer* 2001, 42, 699.